

Electrochemical properties of tetravalent Ti-doped spinel LiMn_2O_4

Lilong Xiong · Youlong Xu · Cheng Zhang ·
Zhengwei Zhang · Jiebin Li

Received: 20 May 2010 / Revised: 4 September 2010 / Accepted: 6 September 2010 / Published online: 23 September 2010
© Springer-Verlag 2010

Abstract Ti-doped spinel LiMn_2O_4 is synthesized by solid-state reaction. The X-ray photoelectron spectroscopy and X-ray diffraction analysis indicate that the structure of the doped sample is $\text{Li}(\text{Mn}^{3+}\text{Mn}^{4+}_{1-x}\text{Ti}^{4+}_x)\text{O}_4$. The first principle-based calculation shows that the lattice energy increases as Ti doping content increases, which indicates that Ti doping reinforces the stability of the spinel structure. The galvanostatic charge–discharge results show that the doped sample $\text{LiMn}_{1.97}\text{Ti}_{0.03}\text{O}_4$ exhibits maximum discharge capacity of 135.7 mAhg^{-1} (C/2 rate). Moreover, after 70 cycles, the capacity retention of $\text{LiMn}_{1.97}\text{Ti}_{0.03}\text{O}_4$ is 95.0% while the undoped sample LiMn_2O_4 shows only 84.6% retention under the same condition. Additionally, as charge–discharge rate increases to 12C, the doped sample delivers the capacity of 107 mAhg^{-1} , which is much higher than that of the undoped sample of only 82 mAhg^{-1} . The significantly enhanced capacity retention and rate capability are attributed to the more stable spinel structure, higher ion diffusion coefficient, and lower charge transfer resistance of the Ti-doped spinel.

Keywords Doping · Capacity retention · Rate capability · Diffusion coefficient · Lithium-ion battery

Introduction

Spiral LiMn_2O_4 is one of the most competitive cathode active materials for the 4-V rechargeable lithium-ion

batteries because of its low cost, abundance in nature, environmental amity, and high safety properties [1–5]. However, LiMn_2O_4 suffers from a fast capacity fade during cycling and especially poor performance at high charge–discharge rate [6, 7], which limits its practical application.

Substituting partial Mn ions with other cations is one of the effective approaches to improve the electrochemical performance of the LiMn_2O_4 [8–17]. The Ti ion-doped $\text{LiMn}_{2-x}\text{Ti}_x\text{O}_4$ compositions have been proposed by many research teams. Specific techniques such as X-ray diffraction [18, 19], electron energy loss spectroscopy [20], X-ray photoelectron spectroscopy [21], electron paramagnetic resonance [22], and neutron powder diffraction [23] are applied to identify the structure and element valence of the compositions. Petrov et al. and Avdeev et al. [22, 24] have reported a new phase in the space group P4₃32 when the compositions fall in the range of $x \geq 1$. Partial occupancy of the tetrahedral sites (8a) by Mn^{2+} ions [25] or Ti^{4+} ions [26] has been reported in the range of $0.2 \leq x \leq 1$. The capacity fade behavior of the $\text{LiMn}_{1.5}\text{Ti}_{0.5}\text{O}_4$ and $\text{Li}[\text{Li}_{0.04}\text{Ti}_{0.49}\text{Mn}_{1.47}]\text{O}_4$ cycling at a higher voltage near 5 V is evaluated by Perentzis et al. [27] and Yang et al. [28], respectively. However, it is reported that, at a higher doping level, excessive volume expansion increases the structure strain which is detrimental to the structure [29], and the increase of the ratio of $\text{Mn}^{3+}/\text{Mn}^{4+}$ leads to the structure distorted [30, 31]. Tong et al. [32] have reported Li poor $\text{Li}_{0.973}\text{Mn}_{1.893}\text{Ti}_{0.048}\text{O}_4$ showing better storage performance. However, a few studies have reported the electrochemical performance of the $\text{LiMn}_{2-x}\text{Ti}_x\text{O}_4$ compositions in the range of $x \leq 0.05$.

In this paper, $\text{LiMn}_{2-x}\text{Ti}_x\text{O}_4$ ($0 \leq x \leq 0.04$) is prepared, aiming to investigate the effect of low content Ti doping on the spiral LiMn_2O_4 . The structure and electrochemical properties of the doped LiMn_2O_4 are investigated in detail.

L. Xiong · Y. Xu (✉) · C. Zhang · Z. Zhang · J. Li
Electronic Materials Research Laboratory, Key Laboratory
of the Ministry of Education, Xi'an Jiaotong University,
Xi'an 710049, People's Republic of China
e-mail: ylxuxjtu@mail.xjtu.edu.cn

Experimental

The $\text{Li}(\text{Mn}_{2-x}\text{Ti}_x)\text{O}_4$ ($0 \leq x \leq 0.04$) samples were prepared by solid-state reaction. All chemical reagents used in the experiments were analytical grade. Stoichiometric amounts of Li_2CO_3 , Mn_3O_4 , and nano- TiO_2 were wet ball-milled for 48 h. The milling intensity was 500 rpm and the ball-to-powder weight ratio was 5:1. After drying, the mixture of starting materials was dry ball-milled for 2 h, then precalcined at 450 °C for 6 h in the air. After slow cooling to room temperature, the calcined powder was grinded by ball milling for 2 h and finally calcined at 750 °C for 12 h.

Analysis of metallic elements content in the samples was characterized by inductively coupled plasma-atomic emission spectrometer (ICP-AES, IRIS-Advantage, Thermo Electron, USA). The manganese average oxidation state in the spinel was determined by potentiometric titration. A bright platinum indicator electrode and a saturated calomel reference electrode were used. About 100 mg of each spinel sample was dissolved in 30 ml of an acidified 0.08 M FeSO_4 solution. During dissolution, all manganese ions were reduced to Mn^{2+} by the Fe^{2+} ions. The excess Fe^{2+} ions in the solution were titrated with 0.04 M KMnO_4 solution. Further titration with the same KMnO_4 solution was carried out to oxidize all Mn^{2+} ions to Mn^{3+} ions. In order to avoid the oxidation to Mn^{4+} , pyrophosphate solution, which is a complexant of the Mn^{3+} ions, was added.

Chemical valence of the titanium element was determined by X-ray photoelectron spectroscopy (XPS) which was performed with an Axis ultra spectrometer (Kratos) using Mono Al K α (1,486.71 eV) radiation at a power of 225 W (15 mA, 15 kV).

The X-ray diffraction (XRD) pattern was recorded using a PANalytical, X'Pert PRO X diffractometer equipped with a Cu-K α radiation ($\lambda=0.15406$ nm) by step scanning. Transmission electron microscopy (TEM; JEM-4000EX, JEOL, Japan) was employed to characterize the prepared powders.

The cyclic voltammograms (CV) and electrochemical impedance spectroscopy (EIS) measurements were tested using Versatile Multichannel Potentiostat 2/Z with the ability for impedance measurements (Bio-logic).

The first principles calculation was performed with the CASTEP code (Materials Studio package), which was based on generalized gradient approximation of density functional theory in the ultrasoft pseudopotential representation, with a plane wave cut-off of 400 eV [33, 34]. The initial crystal model was built based on the experimental data but neglecting the Li/Mn site disorder. The unit cell containing eight formula units was fully relaxed by geometry optimization to adjust the ionic positions and the lattice parameters until the self-consistent field convergence per atom, tolerances for total energy, root-mean-square (RMS) displacement of atoms, RMS force on atoms,

and RMS stress tensor were less than 2×10^{-6} eV, 2×10^{-5} eV, 0.001\AA , 0.05 eV\AA^{-1} , and 0.5 GPa , respectively. Then, the Ti-doped LiMn_2O_4 supercell containing 56 atoms was optimized with Ti replacing the Mn sites. The requested k-point spacing was set as 0.05\AA^{-1} , which corresponded to 32 k-points for LiMn_2O_4 and 8 k-points for Ti-doped LiMn_2O_4 in the irreducible Brillouin zone generated by the Monkhorst–Pack scheme.

For fabrication of $\text{LiMn}_{2-x}\text{Ti}_x\text{O}_4$ electrodes, the prepared powders were mixed with carbon black and polyvinylidene fluoride (70:20:10) in N-methylpyrrolidinone. The slurry thus obtained was coated onto Al foil and then dried at 120 °C overnight in vacuum condition. The electrochemical test cells were assembled in Mikrouna Super glove box under a dry argon atmosphere. $\text{LiMn}_{2-x}\text{Ti}_x\text{O}_4$ electrode was used as positive electrode and Li sheet as negative electrode. Electrolyte was 1 M LiPF_6 dissolved in ethylene carbonate/diethyl carbonate/ethyl methyl carbonate in a 1:1:1 volume ratio.

Charge–discharge characteristics were performed galvanostatically in a cut-off voltage limit of 4.3–3.5 V (vs. Li/Li $^+$) at room temperature by the Arbin Battery Test System.

Results and discussion

ICP-AES is employed to determine the real compositions of the $\text{LiMn}_{2-x}\text{Ti}_x\text{O}_4$ ($x=0.00, 0.01, 0.02, 0.03, 0.04$) samples. The results shown in Table 1 indicate that small Li vacancies exist in the prepared materials, which may be caused by Li_2O volatilization during synthesis [35]. The manganese average oxidation state decreases as the doping content increases, which indicates that the Ti doping increases the ratio of $\text{Mn}^{3+}/\text{Mn}^{4+}$ in the spinel.

Figure 1 shows the XPS spectra of the $\text{LiMn}_{2-x}\text{Ti}_x\text{O}_4$ ($x=0.00$) and $\text{LiMn}_{2-x}\text{Ti}_x\text{O}_4$ ($x=0.03$). Mn, O, and adventitious C elements are observed on the surfaces of both samples while Ti exists only on the surface of the doped sample. The Ti 2p XPS spectrum is shown in Fig. 2. The binding energies of Ti 2p $_{3/2}$ and Ti 2p $_{1/2}$ are 458.2 and 463.8 eV, respectively. The binding energy splitting

Table 1 The real compositions of the $\text{LiMn}_{2-x}\text{Ti}_x\text{O}_4$ samples and the measured average oxidation state of Mn ions

$\text{LiMn}_{2-x}\text{Ti}_x\text{O}_4$	Real compositions	Measured average oxidation state of Mn ions
$x=0.00$	$\text{Li}_{0.997}\text{Mn}_{2.000}\text{O}_{4.000}$	3.502 ± 0.002
$x=0.01$	$\text{Li}_{0.995}\text{Mn}_{1.989}\text{Ti}_{0.011}\text{O}_{4.000}$	3.498 ± 0.002
$x=0.02$	$\text{Li}_{0.994}\text{Mn}_{1.978}\text{Ti}_{0.022}\text{O}_{4.000}$	3.496 ± 0.002
$x=0.03$	$\text{Li}_{0.994}\text{Mn}_{1.970}\text{Ti}_{0.030}\text{O}_{4.000}$	3.494 ± 0.002
$x=0.04$	$\text{Li}_{0.992}\text{Mn}_{1.958}\text{Ti}_{0.042}\text{O}_{4.000}$	3.491 ± 0.002

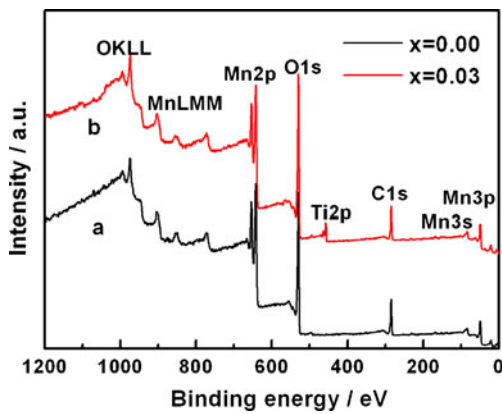


Fig. 1 The XPS spectra of spinel samples. *a* LiMn_2O_4 , *b* $\text{LiMn}_{1.97}\text{Ti}_{0.03}\text{O}_4$

between $2p_{3/2}$ and $2p_{1/2}$ is about 5.6 eV. These results demonstrate that Ti ions in $\text{LiMn}_{2-x}\text{Ti}_x\text{O}_4$ are in the tetravalent oxidation state [36, 37].

The powder XRD patterns of the $\text{LiMn}_{2-x}\text{Ti}_x\text{O}_4$ ($x=0.00, 0.01, 0.02, 0.03, 0.04$) are shown in Fig. 3a. The diffraction peaks of all the samples are identified as a single-phase spinel with a space group Fd3m. For a spinel structure, the (220) peak due to the diffraction of the tetrahedral sites (8a) lies at $2\theta \approx 30.7^\circ$ in the XRD patterns [21, 25]. No (220) peak is observed in Fig. 3a for all the $\text{LiMn}_{2-x}\text{Ti}_x\text{O}_4$ samples. This fact indicates that the Ti ions occupy the octahedral (16d) sites by substituting Mn^{4+} ions, and the tetrahedral sites (8a) are only occupied by lithium ions which give undetectable (220) signals due to their very low X-ray scattering ability. According to the results of the XPS and XRD measurements, it is concluded that the structure of the doped sample is $\text{Li}(\text{Mn}^{3+}\text{Mn}_{1-x}^{4+}\text{Ti}_x^{4+})\text{O}_4$. The doping does not change the spinel LiMn_2O_4 structure. However, it slightly increases the lattice parameters. The lattice parameters of the spinel calculated from the diffraction data are shown in Fig. 3b. The values of the volumes of doped samples slightly increase with increasing

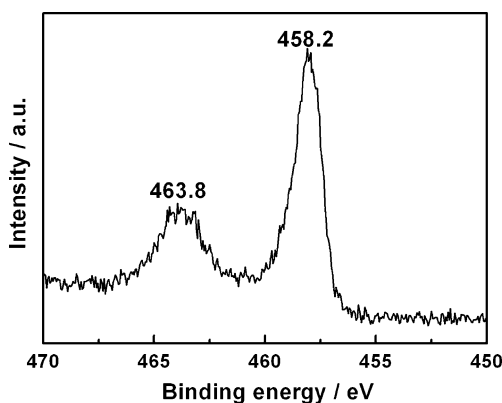


Fig. 2 The XPS spectra of Ti 2p of $\text{LiMn}_{1.97}\text{Ti}_{0.03}\text{O}_4$ spinel

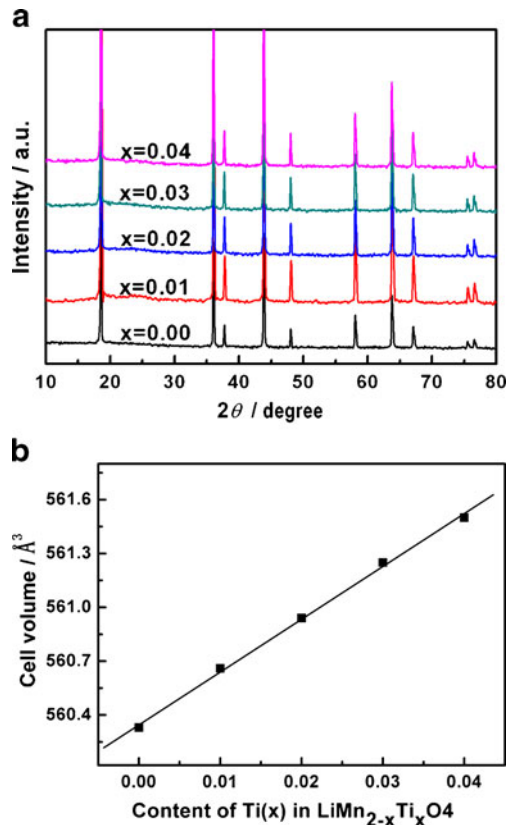


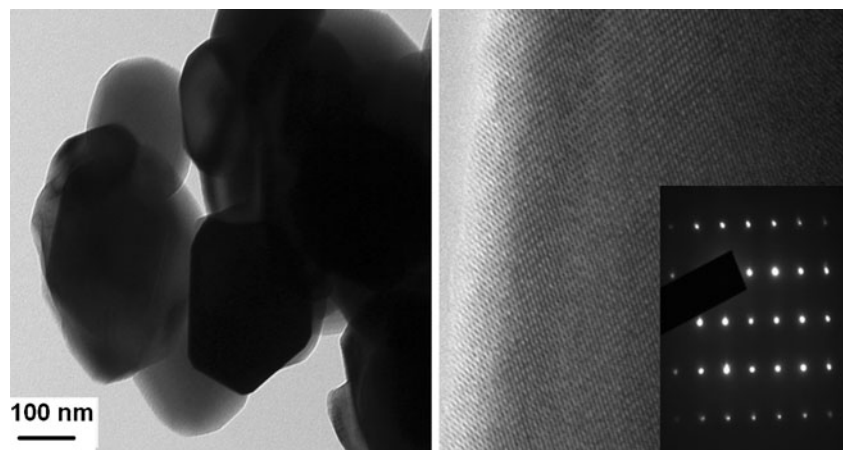
Fig. 3 **a** The XRD patterns of the $\text{LiMn}_{2-x}\text{Ti}_x\text{O}_4$, **b** the cell volumes of $\text{LiMn}_{2-x}\text{Ti}_x\text{O}_4$ samples as a function of the Ti doping content

doping content. This increase is also observed by other research groups [22, 25, 38]; however, the increase in here is slighter than that reported by those groups, which is due to the lower doping content in our experiments. The increase of the lattice parameter may be due to the larger radius of Ti^{4+} (0.061 nm) ions than Mn^{4+} (0.053 nm) ions [39]. According to the results reported by Yang et al. [28], the increase of the ratio of $\text{Mn}^{3+}/\text{Mn}^{4+}$ in the spinel is another factor which leads to the increase of the lattice parameter.

TEM and the corresponding selected area diffraction (SAD) pattern analysis of the $\text{LiMn}_{1.97}\text{Ti}_{0.03}\text{O}_4$ are performed to confirm the chemical homogeneity of the doped samples. As seen in Fig. 4, the $\text{LiMn}_{1.97}\text{Ti}_{0.03}\text{O}_4$ particles with a diameter of about 200 nm are well crystallized and the SAD results show a well-ordered single phase, which indicates that Ti ions are distributed homogeneously in the spinel structure and no impurity phase exists in the doped samples.

Figure 5 shows the discharge profiles of the maximum discharge capacity cycles of $\text{LiMn}_{2-x}\text{Ti}_x\text{O}_4$ ($x=0.00, 0.01, 0.02, 0.03, 0.04$) samples at room temperature. The operating cut-off voltages are 3.5 and 4.3 V at a current rate of C/2. The maximum discharge capacity of LiMn_2O_4 ($x=0.00$) is 138.5 mAhg⁻¹. For the doped samples, the

Fig. 4 The TEM and the corresponding selected area diffraction pattern for the $\text{LiMn}_{1.97}\text{Ti}_{0.03}\text{O}_4$ sample



capacities are 138.1, 136.8, 135.7, and 132.1 mAh g^{-1} as $x=0.01$, 0.02, 0.03, and 0.04, respectively. Two distinct voltage plateaus clearly appear approximately at 4 V on the discharge curve of LiMn_2O_4 ($x=0.00$). It is reported that the higher voltage plateau (region I in Fig. 5) stands for two-phase equilibrium between the $\lambda\text{-MnO}_2$ and $\text{Li}_{0.5}\text{Mn}_2\text{O}_4$ phases while the second plateau (region II in Fig. 5) represents single-phase equilibrium between $\text{Li}_{0.5}\text{Mn}_2\text{O}_4$ and LiMn_2O_4 [40, 41]. The capacity retention could be improved by suppressing the formation of the unstable two cubic phases in region I [42, 43]. For the Ti-doped samples, the boundaries of the two voltage plateaus become unsharp. This may indicate that the Ti doping suppresses the formation of unstable phases and enhances the stability of the spinel structure which is mainly due to the stronger bond of Ti–O (662 kJ mol^{-1}) compared with Mn–O (402 kJ mol^{-1}) [44].

In order to confirm the suppression of the unstable phases, the XRD patterns of LiMn_2O_4 and $\text{LiMn}_{1.97}\text{Ti}_{0.03}\text{O}_4$ which have been extracted from test cells after discharge to 4.1 V (corresponding to region I) are presented in Fig. 6. As shown in the figure, splitting of peaks for the LiMn_2O_4 sample occurs, which strongly indicates that a two-phase structure exists in this region. For the $\text{LiMn}_{1.97}$

$\text{Ti}_{0.03}\text{O}_4$ sample, splitting still exists, but it is much slighter than that of LiMn_2O_4 . This indicates that the Ti doping could suppress the formation of unstable phases though this suppression is not complete due to the low doping content.

The variation of discharge capacity as a function of cycle number for the $\text{LiMn}_{2-x}\text{Ti}_x\text{O}_4$ samples is given in Fig. 7. The undoped sample has the highest capacity, but exhibits poor cycling performance. The capacity decreases rapidly to 117 mAh g^{-1} after 70 cycles with only 84.6% capacity retention. The capacity retention ratios of the doped samples are 91.5%, 93.9%, 95.0%, and 95.4% after 70 cycles as $x=0.01$, 0.02, 0.03, and 0.04, respectively, showing a greatly improved cycling stability with increasing Ti content.

The improved cycling performance is possibly due to the more stable spinel structure caused by Ti doping. The first principles calculation is used to investigate the reason of Ti doping on the improvement of cycling performance. The lattice energies of $\text{LiMn}_{2-x}\text{Ti}_x\text{O}_4$ calculated by the first principles calculation are shown in Fig. 8. Within the appropriate doping range, the lattice energy increases as the doping content increases. This indicates that Ti doping enhances the stability of the lattice structure of the spinel, which is beneficial to improving the capacity retention.

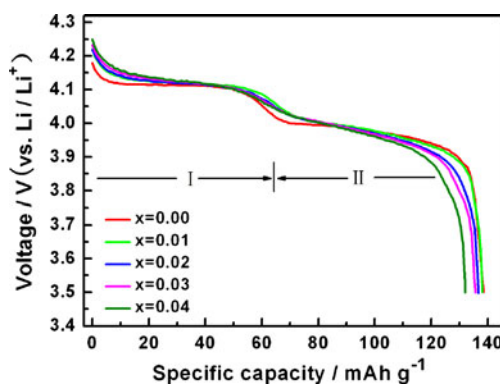


Fig. 5 The discharge profiles of the maximum discharge capacity cycles of the samples

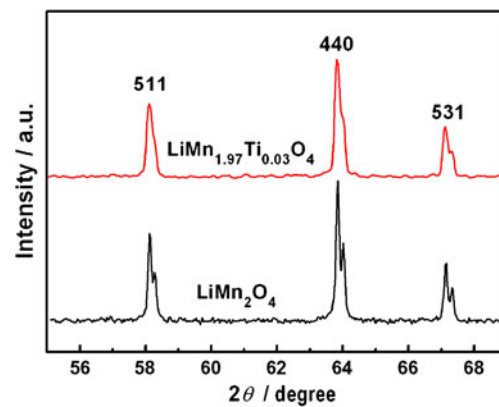


Fig. 6 The XRD patterns measured after discharge to 4.1 V for LiMn_2O_4 and $\text{LiMn}_{1.97}\text{Ti}_{0.03}\text{O}_4$ samples

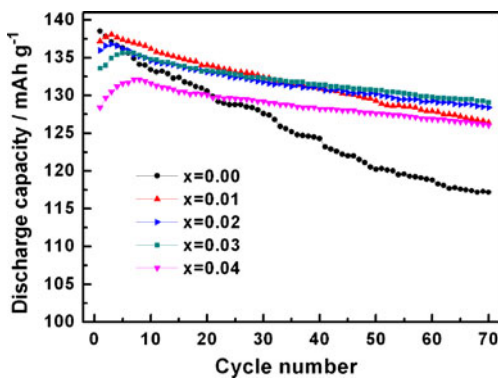


Fig. 7 The variation of discharge capacity as a function of the cycle number of the samples

Figure 9 shows the comparison of the rate capabilities between LiMn_2O_4 and $\text{LiMn}_{1.97}\text{Ti}_{0.03}\text{O}_4$ at the charge–discharge rates ranging from C/2 to 12C. Both materials decrease their capacities with increasing charge–discharge rate, which is caused by the limited diffusion rate of lithium ions in the spinel particles. However, the doped sample delivers much higher capacities than those of the undoped one at high rates. Especially, even at 12C, the doped sample delivers capacity of 107 mAhg^{-1} while the undoped sample delivers only 82 mAhg^{-1} . Moreover, as the charge–discharge rates reduce from 12C to C/2, the doped sample shows a little capacity fade while the undoped sample shows more than 10.9% capacity fade of the seventh cycle at the same rate.

Figure 10a shows the cyclic voltammograms of the $\text{LiMn}_{1.97}\text{Ti}_{0.03}\text{O}_4$ under different scan rates (0.2 – 1.1 mV s^{-1}). It is found that as the scan rate (v) increases, the cathodic and anodic peaks move to lower and higher voltages, respectively, with the increase of the magnitude of peak current (I_p). In the case of semi-infinite and finite diffusion, the peak current I_p is proportional to the square root of the

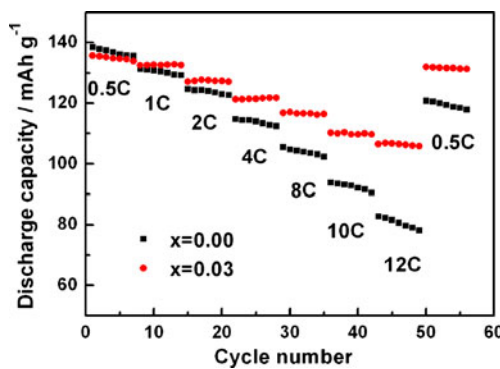


Fig. 9 The discharge capacity vs. cycle number at various charge–discharge rates

scan rate v and accordingly for any separate redox reaction in the plotted CV curve which may be expressed as [45, 46]:

$$I_p = (2.69 \times 10^5)n^{3/2}AD^{1/2}v^{1/2}\Delta C_o, \quad (1)$$

where n is the number of electrons per reaction species (it is 1 for lithium ion), A is the dipped area of the solid-state

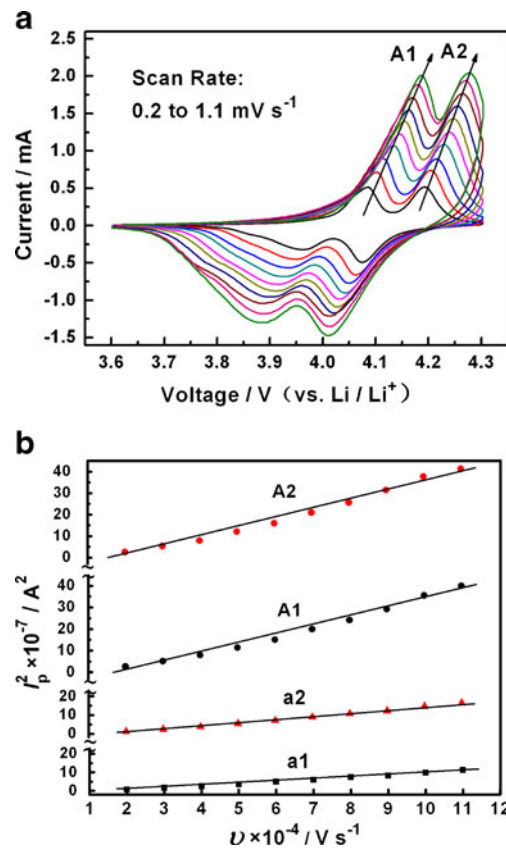


Fig. 10 **a** The cyclic voltammograms of $\text{LiMn}_{1.97}\text{Ti}_{0.03}\text{O}_4$ sample at various scan rates. **b** Plot of the square of peak current (I_p^2) of the cyclic voltammograms vs. v . $A1$ and $A2$, corresponding to the anode peaks of the $\text{LiMn}_{1.97}\text{Ti}_{0.03}\text{O}_4$ sample; $a1$ and $a2$ corresponding to the anode peaks of the LiMn_2O_4 sample which not given in the here. The linear fitting is according to Eq. 2

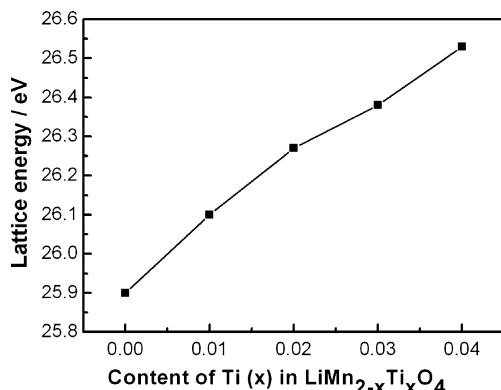


Fig. 8 The lattice energy of $\text{LiMn}_{2-x}\text{Ti}_x\text{O}_4$ samples as a function of the Ti doping content

electrode into the electrolyte solution, D is the diffusion coefficient of Li ion in the electrode, v is the potential scan rate, and ΔC_o is the bulk concentration of Li ion in the electrode. Equation 1 can be transformed as:

$$I_p^2 = (2.69 \times 10^5 \times n^{3/2} \times A \times \Delta C_o)^2 \times D \times v. \quad (2)$$

In the present case, as shown in Fig. 10b, I_p^2 is proportional to v . Calculated from the slope of the linear fit, the diffusion coefficients of $\text{LiMn}_{1.97}\text{Ti}_{0.03}\text{O}_4$ corresponding to A1 and A2 are 1.34×10^{-10} and $1.40 \times 10^{-10} \text{ cm}^2\text{s}^{-1}$, respectively, while those of the LiMn_2O_4 corresponding to a1 and a2 calculated by the same method are 3.80×10^{-11} and $5.40 \times 10^{-11} \text{ cm}^2\text{s}^{-1}$, respectively. Morcrette et al. [47] and Striebel et al. [48] have reported the Li diffusion coefficient of LiMn_2O_4 to be 3.0×10^{-11} and $3.5 \times 10^{-11} \text{ cm}^2\text{s}^{-1}$, respectively. These consistent results indicate that CV measurement is an effective way to determine the Li-ion diffusion coefficient in the spinel. According to the above results, it is believed that partial Mn ion substituted by Ti ion leads to higher Li-ion diffusion coefficient and promotes the Li-ion transport.

The increased ion diffusion coefficient can be explained by: (1) The larger cell size caused by Ti doping is favorable to lithium ion migration. The increased cell size leads to the easier tilting of the M-O₆ octahedron which would reduce the migration resistance of Li ion [49, 50]. (2) The stronger Ti–O bond means the weaker the Li–O bond, and the weaker Li–O bond is favorable to lithium ion migration [51].

Figure 11 shows the EIS of the LiMn_2O_4 and $\text{LiMn}_{1.97}\text{Ti}_{0.03}\text{O}_4$ electrodes. All the measurements are done at 4.1 V within the frequency range of 10 mHz to 1 MHz. The equivalent circuit is presented in Fig. 12, where R_e is the ohmic electrolyte resistance, C_{dl} and R_{ct} are the double-layer capacitance and charge transfer resistance, respectively, W is the finite length Warburg impedance, and C_{int} is the reflection of intercalation capacitance [52]. As seen in

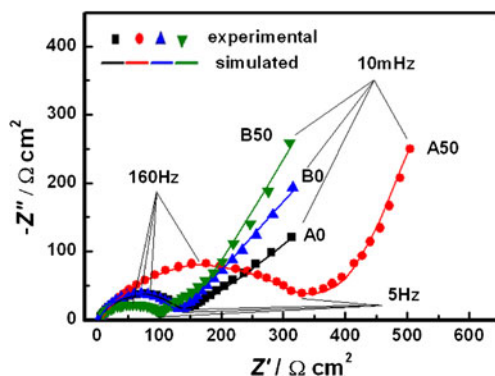


Fig. 11 The electrochemical impedance spectroscopy of the samples. A0: before cycles and A50: after 50 cycles for the LiMn_2O_4 ; B0: before cycles and B50: after 50 cycles for the $\text{LiMn}_{1.97}\text{Ti}_{0.03}\text{O}_4$

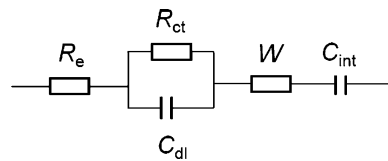


Fig. 12 The equivalent circuit for the electrochemical impedance spectroscopy

Fig. 11, the simulated impedance spectra are well fitted with the experimental ones. The fitting values of the charge transfer resistance (R_{ct}) obtained from EIS are compared in Table 2. The doped sample electrode shows a little smaller charge transfer resistance than that of the undoped sample electrode before cycles. But after 50 cycles, there is a significant difference, where the charge transfer resistance of the doped sample electrode reduces to $96.8 \Omega\text{cm}^2$ while that of the undoped one increases to $315.7 \Omega\text{cm}^2$. The results indicate that lithium intercalation/de-intercalation behavior is harmful to the stability of the spinel; after a few charge–discharge cycles, the damaged spinel makes the charge–transfer reaction at the electrode/electrolyte interface more difficult. However, the Ti doping enhances the lattice stability and the ion diffusion ability in the spinel, which makes the charge transfer reaction easier.

The significant enhancement of the high-rate capability of the Ti-doped sample may be due to the more stable lattice structure, higher Li-ion diffusion coefficient, and lower charge transfer resistance as mentioned above.

Conclusion

The $\text{Li}(\text{Mn}^{3+}\text{Mn}_{1-x}^{4+}\text{Ti}_x^{4+})\text{O}_4$ ($0 \leq x \leq 0.04$) samples have been prepared by solid-state reaction. The doped samples have well-defined spinel structure with tetravalent Ti ion substituting Mn^{4+} ion in the octahedral (16d). The simulation by the first principles shows that the Ti-doped samples have higher lattice energy, which indicates that Ti doping enhances the stability of the spinel structure. The doped sample $\text{LiMn}_{1.97}\text{Ti}_{0.03}\text{O}_4$ exhibits significantly improved capacity retention and much higher capacities even at high rates, which is attributed to the more stable lattice structure, higher ion diffusion coefficient, and lower

Table 2 The fitting values of the charge transfer resistance (R_{ct}) obtained from electrochemical impedance spectroscopy

Sample name	R_{ct} ($\Omega \text{ cm}^2$) before cycles	R_{ct} ($\Omega \text{ cm}^2$) after 50 cycles
LiMn_2O_4	135.3 ± 0.3	315.7 ± 0.3
$\text{LiMn}_{1.97}\text{Ti}_{0.03}\text{O}_4$	132.7 ± 0.3	96.8 ± 0.3

charge transfer resistance. The results of the electrochemical test demonstrate that appropriate tetravalent Ti doping could greatly improve cycling performance and rate capability of the spinel LiMn_2O_4 .

References

1. Gummow RJ, Dekock A, Thackeray MM (1994) Solid State Ionics 69:59–67
2. Jiang CH, Dou SX, Liu HK, Ichihara M, Zhou HS (2007) J Power Sources 172:410–415
3. Kataoka K, Nishimura S, Ogumi Z (2005) J Power Sources 146:217–221
4. Tarascon JM, Armand M (2001) Nature 414:359–367
5. Thackeray MM, Shao-Horn Y, Kahaian AJ, Kepler KD, Vaughey JT, Hackney SA (1998) Electrochim Solid State Lett 1:7–9
6. Inaba M, Doi T, Iriyama Y, Abe T, Ogumi Z (1999) J Power Sources 81–82:554–557
7. Yamada Y, Sagane F, Iriyama Y, Abe T, Ogumi Z (2009) J Phys Chem C 113:14528–14532
8. Idemoto Y, Sekine H, Ui K, Koura N (2005) Solid State Ionics 176:299–306
9. Ito Y, Idemoto Y, Tsunoda Y, Koura N (2003) J Power Sources 119–121:733–737
10. Malyovanyi SM, Andriiko AA, Monko AP (2003) J Solid State Electrochem 8:7–10
11. Mukerjee S, Yang XQ, Sun X, Lee SJ, McBreen J, Ein-Eli Y (2004) Electrochim Acta 49:3373–3382
12. Patoux S, Sannier L, Lignier H, Reynier Y, Bourbon C, Jouanneau S, Le CF, Martinet S (2008) Electrochim Acta 53:4137–4145
13. Singhal R, Das SR, Tomar MS, Ovideo O, Nieto S, Melgarejo RE, Katiyar RS (2007) J Power Sources 164:857–861
14. Suryakala K, Marikkannu KR, Kalaignan GP, Vasudevan T (2007) J Solid State Electrochem 11:1671–1677
15. Thirunakaran R, Kim KT, Kang YM, Seo CY, Young-Lee J (2004) J Power Sources 137:100–104
16. Xiao LF, Zhao YQ, Yang YY, Cao YL, Ai XP, Yang HX (2008) Electrochim Acta 54:545–550
17. Shen PZ, Huang YD, Liu L, Jia DZ, Guo ZP (2006) J Solid State Electrochem 10:929–933
18. Kumar G, Schlorb H, Rahner D (2001) Mater Chem Phys 70:117–123
19. Yoo KS, Cho NW, Oh YJ (1998) Solid State Ionics 113–115:43–49
20. Suzuki S, Tomita M, Okada S, Arai H (1996) J Phys Chem Solids 57:1851–1856
21. Wu QH, Xu JM, Zhuang QC, Sun SG (2006) Solid State Ionics 177:1483–1488
22. Petrov K, Rojas RM, Alonso PJ, Amarilla JM, Lazarraga MG, Rojo JM (2005) Solid State Sci 7:277–286
23. Arillo MA, Cuello G, López ML, Martín P, Pico C, Veiga ML (2005) Solid State Sci 7:25–32
24. Avdeev G, Amarilla JM, Rojo JM, Petrov K, Rojas RM (2009) J Solid State Chem 182:3226–3231
25. Krins N, Hatert F, Traina K, Dusoulier L, Molenberg I, Fagnard JF, Vanderbemden P, Rulmont A, Cloots R, Vertruyen B (2006) Solid State Ionics 177:1033–1040
26. Arillo MA, Lopez ML, Pico C, Veiga ML, Jimenez-Lopez A, Rodriguez-Castellon E (2001) J Alloys Compd 317:160–163
27. Perentzis G, Horopanitis EE, Papadimitriou L (2006) Ionics 12:269–274
28. Shao-Horn Y, Middaugh RL (2001) Solid State Ionics 139:13–25
29. Pistoia G, Antonini A, Rosati R (2001) Chem Mater 9:1443–1450
30. Julien C, Ziolkiewicz S, Lemal M, Massot M (2001) J Mater Chem 11:1837–1842
31. Wolska E, Tovar M, Andrzejewski B, Nowicki W, Darul J, Piszcza P, Knapp M (2006) Solid State Sci 8:31–36
32. Tong QS, Yang Y, Shi JC, Yan J, Zheng LQ (2007) J Electrochem Soc 154:A656–A667
33. Benedek R, Vaughey J, Thackeray MM (2006) Chem Mater 18:1296–1302
34. Van VA, Ceder G (2004) Electrochim Commun 6:1045–1050
35. Arunkumar TA, Alvarez E, Manthiram A (2007) J Electrochem Soc 154:A770–A775
36. Appapillai AT, Mansour AN, Cho J, Shao-Horn Y (2007) Chem Mater 19:5748–5757
37. Lu YC, Mansour AN, Yabuuchi N, Shao-Horn Y (2009) Chem Mater 21:4408–4424
38. Zhang LQ, Yabu T, Taniguchi I (2009) Mater Res Bull 44:707–713
39. Schmidt RL, Verhoeve Jd (1967) Trans Metall Soc AIME 239:148
40. Ohzuku T, Kitagawa M, Hirai T (1990) J Electrochim Soc 137:769–775
41. Xia YY, Yoshio M (1996) J Electrochim Soc 143:825–833
42. Kim KW, Lee SW, Han KS, Chung HJ, Woo SI (2003) Electrochim Acta 48:4223–4231
43. Shen CH, Liu RS, Gundakaram R, Chen JM, Huang SM, Chen JS, Wang CM (2001) J Power Sources 102:21–28
44. Dean JA (1992) Lange's handbook of chemistry, 4th edn. McGraw-Hill, New York
45. Bard AJ, Faulkner LR (2001) Electrochemical methods, 2nd edn. Wiley, New York
46. Das SR, Majumder SB, Katiyar RS (2005) J Power Sources 139:261–268
47. Morcrette M, Barboux P, Perriere J, Brousse T, Traverse A, Boilot JP (2001) Solid State Ionics 138:213–219
48. Striebel KA, Deng CZ, Wen SJ, Cairns EJ (1996) J Electrochim Soc 143:1821–1827
49. Bohnke O, Bohnke C, Fourquet JL (1996) Solid State Ionics 91:21–31
50. Martinez-Juarez A, Pecharroman C, Iglesias JE, Rojo JM (1998) J Phys Chem B 102:372–375
51. Katsumata T, Matsui Y, Inaguma Y, Itoh M (1996) Solid State Ionics 86–8:165–169
52. Levi MD, Aurbach D (1997) J Phys Chem B 101:4630–4640